Three-dimensional spectral element simulations of variable density and viscosity, miscible displacements in a capillary tube

Dirk Wilhelm, Eckart Meiburg *

Department of Mechanical and Environmental Engineering, University of California at Santa Barbara, Santa Barbara, CA 93106, USA

Abstract

A high-accuracy numerical approach is introduced for three-dimensional, time-dependent simulations of variable density and viscosity, miscible flows in a circular tube. Towards this end, the conservation equations are treated in cylindrical coordinates. The spatial discretization is based on a mixed spectral element/Fourier spectral scheme, with careful treatment of the singularity at the axis. For the temporal discretization, an efficient semi-implicit method is applied to the variable viscosity momentum equation. This approach results in a constant coefficient Helmholtz equation, which is solved by a fast diagonalization method. Numerical validation data are presented, and simulations are conducted for the three-dimensionally evolving instability resulting from an unstable density stratification in a vertical tube. Some preliminary comparisons with corresponding experiments are undertaken.
© 2003 Elsevier Ltd. All rights reserved.

1. Introduction

Miscible flows involving fluids of different densities and viscosities are encountered under a wide variety of circumstances, ranging from lubrication applications to enhanced oil recovery. Even in

---

* Corresponding author. Tel./fax: +1-805-893-5278.
E-mail address: meiburg@engineering.ucsb.edu (E. Meiburg).

the simple geometry of a circular pipe, such flows exhibit a range of interesting axisymmetric, helical, and three-dimensional instabilities [1–3], as well as complex non-linear behavior.

The experimental investigations of Petitjeans and Maxworthy [4], and Kuang et al. [5] focus specifically on variable density and viscosity, miscible displacements in capillary tubes at low Reynolds numbers. They show that if a net flow is applied in order to displace a more viscous fluid by a less viscous one, the resulting flow field remains nearly axisymmetric over large parameter ranges. For high Péclet numbers Pe, a quasisteady finger of the less viscous fluid is seen to propagate along the tube axis, leaving behind a layer of the more viscous fluid at the wall. Predominantly axisymmetric behavior is observed regardless of whether the capillary tube is oriented horizontally or vertically. Only in the presence of significant density differences do very slow flows display significant three-dimensional effects. As a result, the early axisymmetric Stokes flow simulations of Chen and Meiburg [6] are able to obtain good overall agreement with the experimental data of Petitjeans and Maxworthy [4] and Kuang et al. [5], as far as the finger propagation velocity and the wall layer thickness are concerned. For small Péclet numbers, on the other hand, there are significant differences between the axisymmetric simulations and the experiments, in that the simulations indicate the formation of a quasisteady finger at a much lower Pe value than the experiments. One possible explanation for this discrepancy could be related to the action of non-conventional, so-called Korteweg stresses [7], which are not accounted for in our earlier simulations [6]. However, preliminary findings by Chen and Meiburg [8] suggest that simple models of these stresses might not be able to fully explain the observed differences. Hence, the possible role of three-dimensional flow effects in this parameter range needs to be explored as well. Due to the small cross section in the experimental capillary tubes, those effects could not be measured quantitatively in [4]. That non-axisymmetric effects can be dominant in certain parameter ranges, however, is clearly demonstrated by Kuang et al. [5] for an unstable density stratification in a vertical pipe, in the absence of a net flow. Already the onset of the instability is seen to be three-dimensional, in that a rising finger of the lighter fluid forms in one half of the tube's cross-section, whereas the heavier fluid begins to fall in the other half. However, these experiments also indicate that a net flow above a certain threshold can stabilize the azimuthal instability mode, so that an axisymmetric mode becomes dominant again.

The above discussion demonstrates a clear need to extend our earlier axisymmetric attempts [6,8] towards high-accuracy, three-dimensional calculations, if a better quantitative understanding of these phenomena is to be achieved. The present work thus aims at developing a suitable computational approach for simulating variable density and viscosity, miscible Stokes flows in capillary tubes. For this purpose, we introduce a highly accurate spatial discretization scheme for a cylindrical coordinate system. A challenge arises because in cylindrical coordinates the momentum and concentration equations exhibit terms containing factors $1/r$ and $1/r^2$, which become singular on the axis for $r \to 0$. Various methods have been proposed in order to remove these singularities on the axis. In the (low order) finite difference context, a flux based formulation in conjunction with a staggered grid is commonly used [9,10] in order to deal with the singularity on the axis. For high order methods, such as spectral or spectral element schemes, the treatment of the singularity requires special care in order to maintain the order of convergence at the axis. When a Fourier spectral scheme is employed in the azimuthal θ-direction, together with a Jacobi polynomial based spectral method in the remaining axial x- and radial r-directions, two approaches are commonly applied. The first choice consists of excluding the discretization of the

points on the axis by using Gauss–Radau points [11] instead of Gauss–Lobatto points, or by employing a special transformation of the Gauss–Lobatto points in the *r*-direction [12]. Alternatively, if the equations are explicitly discretized at the boundary points on the axis, proper boundary conditions for each individual Fourier mode can be derived by L'Hôpital's rule [13–15]. In the present work we employ a spectral element discretization [16] in the axial and radial directions, along with a Fourier spectral scheme in the azimuthal direction. A very detailed and comprehensive overview of axisymmetric spectral element methods is given in the book of Bernardi et al. [17]. Gerritsma and Phillips [18] used an axisymmetric spectral element approach, where they treated the singularities on the axis by means of special expansion functions, based on Jacobi polynomials, in the elements attached to the axis. By exploiting L'Hôpital's rule, these singularities can then be removed. In the present work this approach is extended to a fully three-dimensional discretization scheme in cylindrical coordinate systems.

Our focus is on time-dependent simulations of viscously dominated, miscible displacements. While this allows us to neglect the convective terms in the momentum equation, the corresponding terms in the concentration equation have to be retained. However, the time step restriction due to the viscous terms is much more severe than that resulting from the convective term, cf. [19], so that implicit methods are the preferred choice. This requires the solution of a system of equations for each time step. Since the dimensionless viscosity is of order one, the velocity matrix is much more poorly conditioned than in typical high Reynolds number cases. Moreover, for variable viscosity the evaluation of the stress terms in cylindrical coordinates leads to more then 30 non-linear products that have to be computed in pseudo-spectral fashion [19]. Therefore, with iterative solvers each iteration step becomes significantly more expensive than for constant viscosity, so that efficient direct solvers are desirable. Being a function of concentration, viscosity depends on space and time, and so the application of direct solvers is not straightforward. In the present work, we propose a time-splitting approach for the viscous term, which is at least second order accurate in time and leads to an unconditionally stable discretization with a constant coefficient for the implicit part. This approach is combined with an efficient fast diagonalization solver proposed by Lynch et al. [20] and used by Couzy and Deville [21] in the spectral element framework.

2. Governing equations

We address the problem of the slow displacement of a fluid with dynamic viscosity μ_2 by a second fluid of viscosity μ_1 in an circular tube. The two fluids are assumed to be miscible with each other in all proportions. The numerical simulations to be discussed in the following are intended to shed additional light on the experiments of Petitjeans and Maxworthy [4], and Kuang et al. [5]. In those experiments a suitably defined Reynolds number is $\mathcal{O}(1)$ or less, so that the influence of the convective term in the momentum equations can be neglected. Consequently, the simulations will be based on the incompressible Stokes equations. The relative concentration *c* of the resident fluid 2 is described by a convection–diffusion equation. The governing equations thus read

$$\frac{\partial \underline{u}}{\partial t} - \nabla \cdot \underline{\underline{\tau}}(\mu, \underline{u}) + \nabla p = \rho g \underline{e}_g, \tag{1}$$

$$\nabla \cdot \underline{u} = 0, \tag{2}$$

$$\frac{\partial c}{\partial t} + \underline{u} \cdot \nabla c = D\Delta c. \tag{3}$$

Here $\underline{u} = (u, v, w)$ denotes the fluid velocity vector and its axial, radial and azimuthal components, respectively. $\underline{\tau}$ is the stress-tensor and depends on the velocity and the dynamics viscosity, p indicates pressure, t denotes time, and μ and ρ represent the dynamic viscosity and density, both of which depend on the concentration c. We assume functional relationships of the form

$$\rho(c) = \rho_1 + c(\rho_2 - \rho_1), \quad \mu(c) = \mu_2 e^{R(c-1)}, \quad R = \ln\left(\frac{\mu_2}{\mu_1}\right). \tag{4}$$

The gravitational acceleration g points in the direction of the unit vector $\underline{e}_g$. The diffusion coefficient D is considered constant, which for some fluid combinations represents an approximation. For example, the experiments by Petitjeans and Maxworthy [4] demonstrate a considerable dependence of D on the concentration.

In order to render the above equations dimensionless, all velocities are normalized by a characteristic velocity U, and all lengths are referred to the tube diameter d. A characteristic pressure is provided by $\mu_2 U/d$. Density and viscosity are rendered dimensionless by $\Delta\rho = \rho_1 - \rho_2$ and μ_2, respectively. We thus obtain the non-dimensional equations

$$\frac{\partial \underline{u}}{\partial t} - \nabla \cdot \underline{\tau}(\mu, \underline{u}) + \nabla p = Fc\underline{e}_g, \tag{5}$$

$$\nabla \cdot \underline{u} = 0, \tag{6}$$

$$\frac{\partial c}{\partial t} + \underline{u} \cdot \nabla c = \frac{1}{Pe}\Delta c, \tag{7}$$

where the Péclet number Pe and the gravity number F are defined as

$$Pe = \frac{Ud}{D}, \quad F = \frac{gd^2}{v_2 U}\frac{\Delta\rho}{\rho_2}. \tag{8}$$

Note that the viscosity parameter R can alternatively be expressed as an Atwood number At

$$At = \frac{\mu_2 - \mu_1}{\mu_2 + \mu_1} = \frac{e^R - 1}{e^R + 1}.$$

In the present investigation two different flow configurations will be considered. In the first one, a tube is initially filled with fluid 1 in the upstream half and fluid 2 in the downstream half. A net flow is then applied by injecting fluid 1 at the upstream end, thereby displacing fluid 2. The characteristic velocity U in this case is taken as the centerline velocity of the Poiseuille flow that exists far up- and downstream of the mixed zone. The second configuration consists of a vertically oriented pipe containing two different fluids, without a net flow. Here the flow will be triggered by an instability, if the density stratification is unstable. The characteristic velocity due to buoyancy forces, and the associated Péclet number, can then be defined as

$$U = \frac{gd^2\Delta\rho}{\mu_2}, \quad Pe = \frac{gd^3\Delta\rho}{D\mu_2}. \tag{9}$$

Note that in this case the gravity number F is equal to 1.

3. Computational approach

The governing equations are considered in a cylindrical coordinate system. We first confine our presentation to the axisymmetric case without swirl, for which only the axial and radial directions need to be taken into account. Subsequently, we consider the fully three-dimensional equations.

3.1. Axisymmetric problem

The dimensionless continuity, momentum, and concentration equation for the axisymmetric case are

$$\frac{\partial u}{\partial x} + \frac{1}{r}\frac{\partial}{\partial r}(rv) = 0, \tag{10}$$

$$\frac{\partial u}{\partial t} - \frac{\partial}{\partial x}\tau_{xx} - \frac{1}{r}\frac{\partial}{\partial r}(r\tau_{rx}) + \frac{\partial p}{\partial x} = -Fc, \tag{11}$$

$$\frac{\partial v}{\partial t} - \frac{\partial}{\partial x}\tau_{rx} - \frac{1}{r}\frac{\partial}{\partial r}(r\tau_{rr}) + \frac{\tau_{\theta\theta}}{r} + \frac{\partial p}{\partial r} = 0, \tag{12}$$

$$\frac{\partial c}{\partial t} + u\frac{\partial c}{\partial x} + v\frac{\partial c}{\partial r} - \frac{1}{Pe}\left(\frac{\partial^2 c}{\partial x^2} + \frac{1}{r}\frac{\partial}{\partial r}\left(r\frac{\partial c}{\partial r}\right)\right) = 0. \tag{13}$$

Note that the gravitational term is included only in the case of a vertically oriented tube. The stress-tensor $\underline{\underline{\tau}}$ is defined as

$$\begin{pmatrix} \tau_{xx} & \tau_{xr} & \tau_{x\theta} \\ \tau_{rx} & \tau_{rr} & \tau_{r\theta} \\ \tau_{\theta x} & \tau_{\theta r} & \tau_{\theta\theta} \end{pmatrix} = \mu \begin{pmatrix} 2\frac{\partial u}{\partial x} & \frac{\partial u}{\partial r} + \frac{\partial v}{\partial x} & 0 \\ \frac{\partial u}{\partial r} + \frac{\partial v}{\partial x} & 2\frac{\partial v}{\partial r} & 0 \\ 0 & 0 & 2\frac{v}{r} \end{pmatrix},$$

where u and v denote the velocity components in the x- and r-direction, respectively. Gravity affects only the x-direction.

The spatial discretization of Eqs. (10)–(13) is performed by a spectral element method (SEM). The SEM is based on the decomposition of the computational domain Ω into a number K of non-overlapping subdomains (spectral elements) Ω_k. Each spectral element Ω_k is mapped onto the standard element $\Omega_e = [-1, 1] \times [-1, 1]$, with coordinates e_1, e_2. We employ an iso-parametric mapping, which associates with each point $(e_1, e_2) \in \Omega_e$ a unique point $(x^k, r^k) \in \Omega_k$. In general, the elements Ω_k do not have to be Cartesian, and therefore the coordinates x^k and r^k can be functions of both e_1 and e_2. In the present investigation, however, rectangular elements are advantageous. Consequently, we obtain the simpler relations

$$x^k(e_1) = \xi^k(e_1), \quad r^k(e_2) = \eta^k(e_2),$$

where ξ and η are prescribed functions.

To demonstrate the spectral discretization of the governing equations, we consider as an example the axial momentum equation (11). The weak formulation of Eq. (11) over Ω is

$$\int_{\Omega} \frac{\partial u}{\partial t} \Psi \, \mathrm{d}x r \, \mathrm{d}r + \int_{\Omega} \left(\tau_{xx} \frac{\partial \Psi}{\partial x} + \tau_{rx} \frac{\partial \Psi}{\partial r} - p \frac{\partial \Psi}{\partial x} \right) \mathrm{d}x r \, \mathrm{d}r + B_{\mathrm{T}} = - \int_{\Omega} Fc \Psi \, \mathrm{d}x r \, \mathrm{d}r, \tag{14}$$

where Ψ is the test function and B_{T} is the boundary term due to the integration by parts. The treatment of B_{T} and the implementation of Dirichlet and Neumann boundary conditions require special care in practical applications. We will address this issue in more detail below. Here, we drop the boundary term B_{T} in order to simplify the presentation of the spatial discretization. For a decomposition of Ω into a number of spectral elements K, we can transform the weak forms of the individual elements on the standard element and obtain

$$\int_{\Omega_e} \frac{\partial u}{\partial t} \Psi |\underline{\underline{J}}| r \, \mathrm{d}e_1 \, \mathrm{d}e_2 + \int_{\Omega_e} \left(\tau_{xx} \frac{\partial \Psi}{\partial e_1} \frac{\mathrm{d}r}{\mathrm{d}e_2} + \tau_{rx} \frac{\partial \Psi}{\partial e_2} \frac{\mathrm{d}x}{\mathrm{d}e_1} - p \frac{\partial \Psi}{\partial e_1} \frac{\mathrm{d}r}{\mathrm{d}e_2} \right) |\underline{\underline{J}}| r \, \mathrm{d}e_1 \, \mathrm{d}e_2$$

$$= - \int_{\Omega_e} Fc \Psi |\underline{\underline{J}}| r \, \mathrm{d}e_1 \, \mathrm{d}e_2, \tag{15}$$

where $|\underline{\underline{J}}|$ is the determinant of the Jacobi matrix associated with the iso-parametric mapping (see [27]).

To ensure compatibility between the discrete velocity and pressure space, we use the $P_N - P_{N-2}$ method of Maday and Patera [16]. Within each spectral element, the solutions for velocity and pressure are expanded in tensor-product-based polynomials of order N (velocity) and $N-2$ (pressure), respectively. The expansion functions for the velocity in the x-direction can be expressed in terms of the one-dimensional Lagrangian interpolating polynomials based on the $N+1$ Gauss–Lobatto–Legendre nodes (GLL). For the pressure expansion functions, they are based on the one-dimensional Lagrangian interpolating polynomial through the $N-1$ Gauss–Legendre (GL) nodes. Following Tomboulides [14] or Gerritsma and Phillips [18], the expansion basis in the r-direction is different for the elements adjacent to the axis and the remaining elements. In the former, we use interpolation functions through the $N+1$ Gauss–Lobatto–Jacobi points (GLJ) for the velocity. For the pressure, we consider interpolation functions through the $N-1$ Gauss–Jacobi (GJ) points, which are associated with the Jacobi polynomials $P^{(0,1)}$. In the latter, we use the same expansion functions in the r-direction as in the x-direction. Note that Gerritsma and Phillips [18] employ the non-staggered approach, in which the pressure is discretized at the $N-1$ inner velocity points.

The expansions of the axial velocity u and the pressure p in an element adjacent to the axis read

$$u(x,r) = \sum_{i,j=0}^{N} u_{ij} \phi_i(e_1) \bar{\phi}_j(e_2), \tag{16}$$

$$p(x,r) = \sum_{i,j=1}^{N-1} p_{ij} \psi_i(e_1) \bar{\psi}_j(e_2), \tag{17}$$

where ϕ_i and ψ_i are the Lagrange interpolation functions associated with the GLL and GL points, respectively. The interpolation functions associated with the GLJ and GJ points are denoted by $\bar{\phi}_j$ and $\bar{\psi}_j$. Note that the test functions Ψ are expanded in the same manner as the velocity. If we

introduce these expansions into the weak from of Eq. (15), and consider the second term of this equation as an example, we obtain for constant viscosity μ

$$\int_{\Omega_e} 2\mu \sum_{i,j=0}^{N} \phi_i'(e_1)\bar{\phi}_j(e_2)u_{ij} \sum_{r,s=0}^{N} \phi_r'(e_1)\bar{\phi}_s(e_2)\Psi_{rs} \frac{\mathrm{d}r}{\mathrm{d}e_2} \frac{r(e_2)}{w(e_2)} |\underline{\underline{J}}|w(e_2)\,\mathrm{d}e_1\,\mathrm{d}e_2, \tag{18}$$

where $\phi_i'(e_1)$ denotes the derivative with respect to e_1. Note that we multiplied the equation by $w(e_2)/w(e_2)$, where $w(e_2) := (1 + e_2)$ is the weight function associated with the Jacobi polynomial $P^{(0,1)}$ (cf. [14,18,19]). We assume, without loss of generality, that the side that corresponds to the symmetry axis is mapped onto the edge $e_2 = -1$ of Ω_e. Then numerator and denominator of the fraction r/w tend to zero for $r \rightarrow 0$, and we apply L'Hôpital's rule at the axis. This gives

$$\left.\frac{r(e_2)}{w(e_2)}\right|_{e_2=-1} = \frac{\partial r(e_2)}{\partial e_2}.$$

The integral of Eq. (18) is evaluated by GLL and GLJ quadrature [19] in e_1- and e_2-directions, respectively

$$\sum_{p,q=0}^{N} 2\mu \sum_{i,j=0}^{N} \phi_i'(e_{1,p})\bar{\phi}_j(e_{2,q})u_{ij} \sum_{r,s=0}^{N} \phi_r'(e_{1,p})\bar{\phi}_s(e_{2,q})\Psi_{rs} \frac{\mathrm{d}r}{\mathrm{d}e_2} \frac{r(e_2)}{w(e_2)} |\underline{\underline{J}}|w_p\bar{w}_q,$$

where w_p denotes the GLL weight. The function $w(e_2)$ is absorbed into the GLJ weights $\bar{w}_q$ (cf. [18]). The first and the third terms of Eq. (15) are dealt with in the same manner. The treatment of the pressure term (the last term) in this equation is even simpler, because pressure is not discretized at the axis of symmetry due to the staggered grid.

In the axisymmetric case the physical boundary conditions on the axis are

$$\frac{\partial u}{\partial r} = 0 \quad \text{and} \quad v = 0. \tag{19}$$

The boundary term B_T of the axial momentum equation (14) is

$$B_\mathrm{T} = -\int_{\partial\Omega} \mu\Psi \frac{\partial u}{\partial r}\,\mathrm{d}s + \int_{\partial\Omega} p\,\mathrm{d}s.$$

The Dirichlet boundary condition ($v = 0$) is employed as essential boundary condition, i.e., it is implemented directly in the approximation space. In contrast, the Neumann boundary condition ($\partial u/\partial n = 0$) is considered as natural boundary condition in the weak form. This approach is common in finite element methods (cf. [22]). Employing the same procedure to Eqs. (10), (12) and (13) yields a semi-discretized system for velocity, pressure and concentration. If the viscosity μ varies with concentration, $\mu(x, r, t)$ is expanded in the same manner as the axial velocity u, and the relation (4) is employed to close the problem.

3.2. Temporal discretization of the axisymmetric problem

The semi-discretized system is now discretized in time. We first consider only the momentum (5) and continuity (6) equations

$$\frac{\partial \underline{u}_N}{\partial t} + \underline{\underline{L}}(\mu)\underline{u}_N - \underline{\underline{D}}^T p_N = \underline{\underline{B}}\underline{f}_N,\tag{20}$$

$$\underline{\underline{D}}\underline{u}_N = 0,\tag{21}$$

where $\underline{\underline{L}}(\mu)$ is the discrete spatial diffusion operator, $\underline{\underline{D}}^T$ denotes the discrete gradient operator, $\underline{\underline{D}}$ the discrete divergence operator, and $\underline{\underline{B}}$ represents the discrete mass matrix. Furthermore, $\underline{u}_N$ and p_N indicate velocity and pressure, respectively, while $\underline{f}_N$ denotes the right-hand-side at the nodal points. Note that $\underline{f}_N$ is a function of the concentration, and that $\underline{\underline{L}}(\mu)$ depends on the viscosity.

The time step restriction due to the diffusive term in the Stokes equation is much more severe than the CFL criterion imposed by the convective term in the convection–diffusion equation (7). Consequently, it is desirable to treat the diffusive term in the Stokes equation implicitly. Towards this end, we employ a second order backward differentiation method (*BDF*2), cf. [23]

$$\left(\frac{3}{2\Delta t}\underline{\underline{B}} + \underline{\underline{L}}(\mu)\right)\underline{u}_N^{n+1} - \underline{\underline{D}}^T p_N^{n+1} = \underline{\underline{B}}\underline{f}_N^{n+1} + \frac{1}{\Delta t}\left(2\underline{\underline{B}}\underline{u}_N^n - \frac{1}{2}\underline{\underline{B}}\underline{u}_N^{n-1}\right),\tag{22}$$

$$\underline{\underline{D}}\underline{u}_N^{n+1} = 0,\tag{23}$$

where the superscript n denotes a quantity at time $t^n := n \cdot \Delta t$. One possibility is to use the Uzawa algorithm [24] to solve this system of equations. However, here we employ the more efficient fractional step method proposed by Maday et al. [25] instead. This method takes the form

$$\left(\frac{3}{2\Delta t}\underline{\underline{B}} + \underline{\underline{L}}(\mu)\right)\underline{u}_N^* = \underline{g}_N^n + \underline{\underline{D}}^T p_N^n,\tag{24}$$

$$\frac{2\Delta t}{3}\underline{\underline{D}}\,\underline{\underline{B}}^{-1}\underline{\underline{D}}^T \delta p_N = -\underline{\underline{D}}\,\underline{u}_N^*,\tag{25}$$

$$\underline{u}_N^{n+1} = \frac{2\Delta t}{3}\underline{\underline{B}}^{-1}\underline{\underline{D}}^T \delta p_N + \underline{u}_N^*,\tag{26}$$

where $\underline{u}^*$ is a splitting velocity that is evaluated from Eq. (24), $\delta p_N := p_N^{n+1} - p_N^n$ represents the pressure deviation, and $\underline{g}_N^n$ denotes the right-hand-side of Eq. (22). In Eqs. (24)–(26) a splitting error is involved that is of second order in Δt [26]. Note that one Helmholtz equation (24) and one so-called "pseudo-Laplacian" equation (25) have to be solved at each time step. The pressure equation (25) is usually ill-conditioned, which renders direct solvers [27] or very sophisticated preconditioned iterative solvers [28] desirable. Here we use a direct solver that is based on the fast diagonalization method of Lynch et al. [20] (for a short overview of this method see Appendix A.1). This method has been applied to the spectral element pressure matrix in [27], and has been proven to be at least an order of magnitude faster than a preconditioned conjugate gradient solver. The condition number of the Helmholtz operator is a function of $\kappa = 3/(2\Delta t\mu)$. If κ increases, the condition number tends to unity, and the Helmholtz matrix becomes diagonally dominant. For high Reynolds number flows κ is usually large, and hence the Helmholtz matrix is well-conditioned. Under those circumstances iterative solvers converge very rapidly. In the present case, however, the Helmholtz matrix is ill-conditioned, so that direct solvers become the preferred choice. A very efficient direct solver is the fast diagonalization solver mentioned above. This approach can be

employed to the Helmholtz matrix if μ is constant (cf. [21]). The basic idea behind the fast diagonalization solver is to compute an eigenvalue decomposition of the Helmholtz operator in a preprocessing step. Subsequently, the inverse of the decomposed operator is computed and stored. To evaluate the solution of the Helmholtz equation, only multiplications have to be performed. However, the preprocessing step is appropriate only for time-independent Helmholtz operators, so that we aim at obtaining such an operator even for the variable viscosity problem.

Let us consider the fully discretized momentum equation (22) in the form

$$\left(\frac{3}{2\Delta t}\underline{\underline{B}}\right)\underline{u}_N^{n+1} - \underline{\underline{D}}^T p_N^{n+1} = \underline{g}_N^n - \underline{\underline{L}}(\mu)\underline{u}_N^{n+1}. \tag{27}$$

We define the diffusive operator associated with the maximum viscosity $\mu_{\max} = \max(\mu(x,r,t))$ as $\underline{\underline{L}}^{\max}$. Note that $\mu_{\max}$ is time-independent and can be determined as an upper bound of μ at the start of the simulation. We can add $\underline{\underline{L}}^{\max}\underline{u}_N^{n+1}$ on both sides of Eq. (27)

$$\left(\frac{3}{2\Delta t}\underline{\underline{B}} + \underline{\underline{L}}^{\max}\right)\underline{u}_N^{n+1} - \underline{\underline{D}}^T p_N^{n+1} = \underline{g}_N^n + \left(\underline{\underline{L}}^{\max} - \underline{\underline{L}}(\mu)\right)\underline{u}_N^{n+1},$$

and approximate the term $(\underline{\underline{L}}^{\max} - \underline{\underline{L}}(\mu))\underline{u}_N^{\max}$ by a second order extrapolation method (EX2), which results in a second order semi-implicit method

$$\left(\frac{3}{2\Delta t}\underline{\underline{B}} + \underline{\underline{L}}^{\max}\right)\underline{u}_N^{n+1} - \underline{\underline{D}}^T p_N^{n+1} = \underline{g}_N^n + 2\left(\underline{\underline{L}}^{\max} - \underline{\underline{L}}(\mu)\right)\underline{u}_N^n - \left(\underline{\underline{L}}^{\max} - \underline{\underline{L}}(\mu)\right)\underline{u}_N^{n-1}. \tag{28}$$

In Appendix A.2 we show for a simplified test problem that the semi-implicit method is unconditionally stable. The Helmholtz operator on the left-hand-side is time-independent, and thus this Helmholtz equation can be solved by employing the direct fast diagonalization solver [20,21].

We are now in a situation to present the fully discretized system of Eqs. (10)–(13). Towards this end, the concentration equation (13) is discretized by a mixed implicit/explicit time stepping scheme. We use a BDF2 method for the diffusive term and an EX2 method of the convective term. Finally we obtain

$$\left(\frac{3}{2\Delta t}\underline{\underline{B}} + \underline{\underline{L}}_c\right)c_N^{n+1} = \frac{1}{\Delta t}\left(2\underline{\underline{B}}c_N^n - \frac{1}{2}\underline{\underline{B}}c_N^{n-1}\right) + 2\underline{\underline{N}}(\underline{u}_N^n)c_N^n - \underline{\underline{N}}(\underline{u}_N^{n-1})c_N^{n-1}, \tag{29}$$

$$\mu_N^{n+1} = e^{R(c_N^{n+1}-1)}, \tag{30}$$

$$\left(\frac{3}{2\Delta t}\underline{\underline{B}} + \underline{\underline{L}}^{\max}\right)\underline{u}_N^{n+1} - \underline{\underline{D}}^T p_N^{n+1} = \underline{g}_N^n + 2\left(\underline{\underline{L}}^{\max} - \underline{\underline{L}}(\mu_N^{n+1})\right)\underline{u}_N^n - \left(\underline{\underline{L}}^{\max} - \underline{\underline{L}}(\mu_N^{n+1})\right)\underline{u}_N^{n-1}, \tag{31}$$

$$\underline{\underline{D}}\,\underline{u}_N^{n+1} = 0, \tag{32}$$

where $\underline{\underline{L}}_c$ and $\underline{\underline{N}}(\underline{u}_N^n)$ are the discretized diffusion and convection operators of the concentration equation, respectively. The computation of the nth time step is now performed in the following way: First, the concentration equation is solved using the old velocity and concentration values. It should be noted that here we use the same efficient fast diagonalization solver as for the momentum equation. Subsequently, the viscosity μ_N^{n+1} is updated directly from c_N^{n+1}. Finally, the

momentum and continuity equation are solved together by employing the fractional step method according to Eqs. (24)–(26).

4. Axisymmetric flow simulations

4.1. Validation

In order to validate the method described above, we establish the second order accuracy in Δt of the semi-implicit algorithm by means of comparing with an analytic solution. Furthermore, we reproduce the miscible flow results of Chen and Meiburg [6] in a capillary tube.

We consider the axisymmetric problem of the form

$$\frac{\partial \underline{u}}{\partial t} - \nabla(\mu \nabla \underline{u}) + \nabla p = \underline{f}, \tag{33}$$

$$\nabla \cdot \underline{u} = 0, \tag{34}$$

$$\frac{\partial c}{\partial t} + \underline{u} \cdot \nabla c - \frac{1}{Pe} \Delta c = f_c \tag{35}$$

with exact solution $(\underline{u} := (u, v))$

$$u(x, r, t) = x^3 r^2 \cos(t), \tag{36}$$

$$v(x, r, t) = -\frac{3}{4} x^2 r^3 \cos(t), \tag{37}$$

$$p(x, r, t) = x^2 r^2 \cos(t), \tag{38}$$

$$\mu(x, r, t) = e^{(ax+br)}, \tag{39}$$

where a and b are given constants and the forcing terms $\underline{f} = (f_x, f_r), f_c$ are chosen such that Eqs. (33)–(35) are fulfilled. We solve the equations on the domain $\Omega = [0, 1] \times [0, 1]$ and prescribe the exact solution as Dirichlet conditions on the boundary of the domain.

We begin by considering the special case $a = b = 0$, for which μ is constant, and 2×2 elements are employed, with a time step $\Delta t = 10^{-4}$. The spectral convergence of the SEM is apparent from Fig. 1, which shows the maximum error in the computational domain. As a further test, we keep the polynomial degree constant and compare the error of the constant viscosity case with that for a variable viscosity one ($a = 0.1, b = 0.2$), cf. Fig. 2. The error is almost identical for both cases.

The second order accuracy in time is clearly demonstrated by the figure. This shows that the splitting error introduced by the semi-implicit operator splitting is also of second order in Δt.

4.2. Results

As a further validation step, we compare numerical results obtained by the present approach with earlier ones of Chen and Meiburg [6]. We consider a pipe whose upstream half is filled with
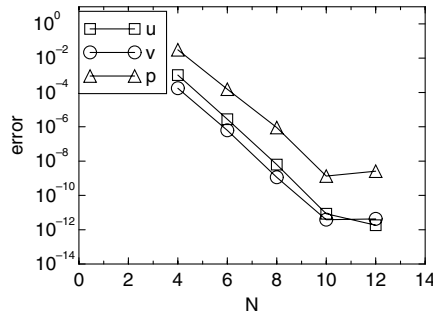
Fig. 1. Maximum error as a function of the polynomial degree N. Stokes flow with constant viscosity ($\mu = 1$). The results demonstrate spectral convergence.
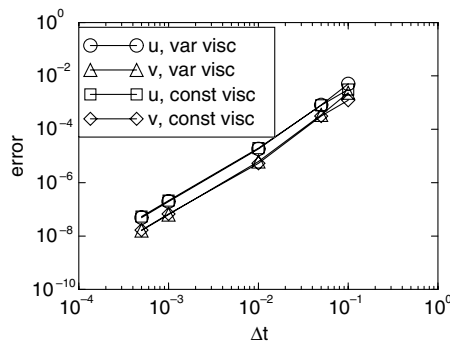

Fig. 2. Maximum error as a function of the time step. Comparison of constant viscosity and variable viscosity cases. The results indicate second order accuracy in time for both cases.

fluid 1, while fluid 2 occupies the downstream half. The fluids are miscible and have different viscosities μ_1 and μ_2 with $\mu_2 > \mu_1$. At time $t = 0$, a net flow is generated by which fluid 1 displaces fluid 2. The flow is characterized by the Péclet number Pe, the viscosity contrast R, and the gravity number F as defined in (8). In order to be able to compare, we take the same parameter values as Chen and Meiburg [6], i.e., $Pe = 1600$, $R = 5$, and $F = 0$. Since the concentration front propagates downstream with a certain tip velocity V_{tip}, we perform the simulations in a moving frame of reference. The computational domain extends from 0 to 1.5 in the axial direction, and from 0 to 0.5 in the radial direction. We prescribe the symmetry conditions (19) at the axis and no-slip conditions at the solid wall. In the moving reference frame, the 'downstream' boundary at $x = 1.5$ becomes an inflow boundary. Here, we assume a Poiseuille flow velocity profile, which is a good approximation as long as care is taken to keep this boundary sufficiently far removed from the propagating front. The 'upstream' boundary at $x = 0$ becomes a mixed inflow/outflow boundary in the moving reference frame. Here we apply a convective boundary condition of the following form for the concentration

$$\frac{\partial c}{\partial t} + V \frac{\partial c}{\partial x} = 0.$$

This condition is discretized in space and time

$$\frac{\underline{\underline{B}} c_N^{n+1} - \underline{\underline{B}} c_N^n}{\Delta t} + V \underline{\underline{D}}_x c_N^n = 0,$$

where $\underline{D}_x$ is the SEM derivative operator in the x-direction, and $\underline{B}$ denotes the (diagonal) mass matrix. For test purposes, we implemented a wide range of convection velocities V in the above boundary condition. The simulation results were found to be nearly independent of the value of V. For the velocity, we employ a homogeneous Neumann condition. The spatial resolution is 32×4 elements of polynomial degree $N = 8$, with a time step of $\Delta t = 0.5 \times 10^{-3}$.

In Fig. 3 the concentration contours (at levels $c = 0.1, 0.2, \ldots, 0.9$) are given for $t = 1$ and 3. The comparison with the results of Chen and Meiburg [6] in Fig. 4 indicates good quantitative agreement. Note that different values were taken for the velocities of the moving reference frame in the two simulations. Consequently, only the shape, but not the location of the concentration contours should be compared. The concentration front is seen to propagate downstream with a time dependent tip velocity $V_{tip}(t)$. Following Chen and Meiburg [6], we define V_{tip} as the rate at which the concentration contour $c = 0.5$ propagates. In Fig. 5 $V_{tip}(t)$ is plotted as a function of time. After an initial transient of about two dimensionless time units, V_{tip} approaches a constant value which closely matches that of [6]. The discrepancies between the simulations during the transient phase are due to the fact that different initial front thicknesses were employed. As a result, only the long time asymptotic values of $V_{tip}(t)$ should be compared. The accompanying streamline pattern in the frame of reference moving with V_{tip} shows the existence of a stagnation point at the tip, cf. Fig. 6, which is in agreement with [6]. Note that we also performed a simulation on a much finer grid of 50×6 elements ($N = 8$) and found virtually no difference compared to the coarser grid results. Furthermore, we performed a simulation in a domain four times as long in the axial direction, which again gave essentially identical results.
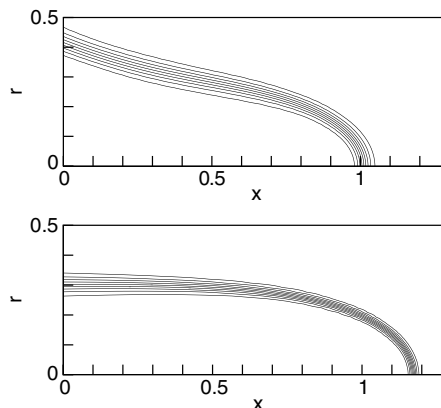

Fig. 3. Concentration contours at $t = 1$ and 3 of the axisymmetric simulation for $Pe = 1600$, $R = 5$, and $F = 0$. Good agreement with the axisymmetric simulation results of Chen and Meiburg [6] is observed, cf. Fig. 4.
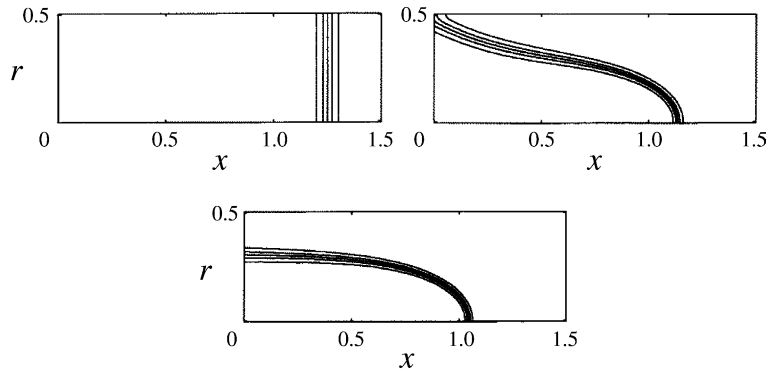
Fig. 4. Concentration contours taken from the axisymmetric simulations of Chen and Meiburg [6] at $t = 0, 1$ and 3, for the same parameter values as in Fig. 3.
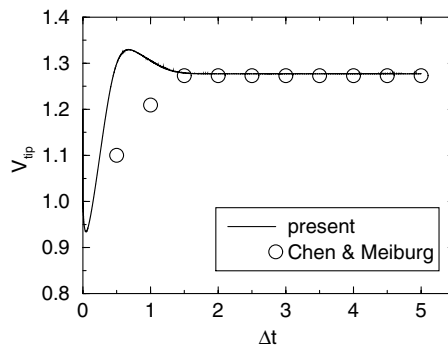

Fig. 5. Comparison of the tip velocity V_{tip} with the numerical results of Chen and Meiburg [6]. $Pe = 1600$, $R = 5$, and $F = 0$. Good agreement is observed for the long time asymptotic values.
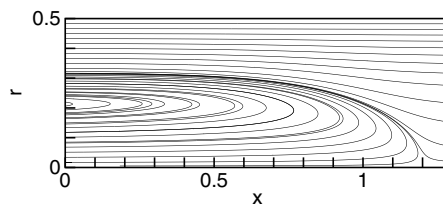

Fig. 6. Streamlines of the axisymmetric simulation in the moving reference frame, $Pe = 1600$, $R = 5$, and $F = 0$.

5. Three-dimensional flow simulations

Here we consider the stability problem in which a heavier fluid is located above a lighter one in a vertical pipe, in the absence of a net flow. For this case, the characteristic velocity due to buoyancy forces, along with the associated Péclet number, are defined by Eq. (9). The gravity parameter is $F = 1$ for this case. The spatial discretization of the governing equations (4)–(7) is again performed in a cylindrical coordinate system. The axial, radial, and azimuthal directions are

denoted by x, r, and θ, and the respective velocity components are (u, v, w). We employ a Fourier spectral expansion in the azimuthal direction

$$\underline{u}(x, r, \theta, t) = \sum_{m=0}^{N_z/2-1} \underline{\hat{u}}_m(x, r, t)e^{im\theta}, \tag{40}$$

where m represents the azimuthal Fourier mode. Furthermore, we introduce the new variables

$$\tilde{v}_m = \hat{v}_m + i\hat{w}_m, \quad \tilde{w}_m = \hat{v}_m - i\hat{w}_m \tag{41}$$

following to Tomboulides [14] or Tomboulides and Orszag [15]. These authors show that, close to the axis, the Fourier coefficients of the velocity components behave as

$$(\hat{u}_m, \hat{v}_m, \hat{w}_m) \propto (\beta r^m, \gamma r^{m-1}, i\gamma r^{m-1}), \tag{42}$$

where β and γ are constants. They furthermore demonstrate that $\tilde{v}_m$ vanishes at $r = 0$ and scales like $\tilde{v}_m \propto r^{m+1}$, which is equivalent to the fact that the vorticity is regular at $r = 0$. On the other hand, the variable $\tilde{w}_m$ has a non-zero value at $r = 0$ for $m = 1$. However, Tomboulides and Orszag [15] show that for $m = 1$ the $1/r^2$ terms vanish in the azimuthal momentum equation. Hence, the singularity at $r = 0$ can be removed by the transformation (41).

However, there are still terms in the equations for which both numerator and denominator go to zero at the same rate close to the axis, which leads to equations of undetermined forms. To handle this problem, we employ the same special treatment as in the axisymmetric case (cf. Section 3.1). Moreover, boundary conditions are required at the axis, if a SEM discretization is employed in the (x, r)-plane. These conditions, which can be deduced from the continuity equation and the relation (42) according to [14,29], are summarized in Table 1.

5.1. Spatial and temporal discretization

For the sake of simplicity, we consider in a first step Stokes flow with constant viscosity and density. Then the pressure and the forcing term $\underline{f} = (f_x, f_r, f_\theta)$ can be expanded similarly to the velocity (40). By introducing these expansions into Eqs. (5) and (6), we obtain one system of equations for each of the $N_z/2$ complex Fourier modes by using the transformation (41)

$$\frac{\partial \hat{u}_m}{\partial t} - \mu \left(\Delta_{xr} - \frac{m^2}{r^2} \right) \hat{u}_m + \frac{\partial \hat{p}_m}{\partial x} = \hat{f}_{m,x}, \tag{43}$$

Table 1
Boundary conditions at the axis $r = 0$ for different Fourier modes

	$m = 0$	$m = 1$	$m \geqslant 2$
$\hat{u}_m$	$\partial \hat{u}_m/\partial r = 0$	$\hat{u}_m = 0$	$\hat{u}_m = 0$
$\hat{v}_m$	$\hat{v}_m = 0$	$\partial \hat{v}_m/\partial r = 0$	$\hat{v}_m = 0$
$\hat{w}_m$	$\hat{w}_m = 0$	$\partial \hat{w}_m/\partial r = 0$	$\hat{w}_m = 0$
$\hat{c}_m$	$\partial \hat{c}_m/\partial r = 0$	$\hat{c}_m = 0$	$\hat{c}_m = 0$
$\tilde{v}_m$	$\tilde{v}_m = 0$	$\tilde{v}_m = 0$	$\tilde{v}_m = 0$
$\tilde{w}_m$	$\tilde{w}_m = 0$	$\partial \tilde{w}_m/\partial r = 0$	$\tilde{w}_m = 0$

$$\frac{\partial \tilde{v}_m}{\partial t} - \mu \left(\Delta_{xr} - \frac{(m+1)^2}{r^2} \right) \tilde{v}_m + \frac{\partial \hat{p}_m}{\partial r} - \frac{m}{r} \hat{p}_m = \tilde{f}_{m,r}, \tag{44}$$

$$\frac{\partial \tilde{w}_m}{\partial t} - \mu \left(\Delta_{xr} - \frac{(m-1)^2}{r^2} \right) \tilde{w}_m + \frac{\partial \hat{p}_m}{\partial r} + \frac{m}{r} \hat{p}_m = \tilde{f}_{m,\theta}, \tag{45}$$

$$\frac{\partial \hat{u}_m}{\partial x} + \frac{1}{2r} \frac{\partial (r\tilde{v}_m)}{\partial r} + \frac{m\tilde{v}_m}{2r} + \frac{1}{2r} \frac{\partial (r\tilde{w}_m)}{\partial r} - \frac{m\tilde{w}_m}{2r} = 0, \tag{46}$$

where

$$\Delta_{xr} = \frac{\partial^2}{\partial x^2} + \frac{1}{r} \frac{\partial}{\partial r} \left(r \frac{\partial}{\partial r} \right), \tag{47}$$

$$\tilde{f}_{m,r} = \hat{f}_{m,r} + i\hat{f}_{m,\theta}, \tag{48}$$

$$\tilde{f}_{m,\theta} = \hat{f}_{m,r} - i\hat{f}_{m,\theta}. \tag{49}$$

Here $\hat{p}_m$, $\hat{f}_{m,x}$, $\hat{f}_{m,r}$, and $\hat{f}_{m,\theta}$ refer to the Fourier coefficients of p and the components of $\underline{f}$, respectively. Now we consider as an example the variational form according to $\tilde{v}_m$

$$\int_\Omega \frac{\partial \tilde{v}_m}{\partial t} \Psi \, \mathrm{d}xr \, \mathrm{d}r + \int_\Omega \mu \left(\frac{\partial \tilde{v}_m}{\partial x} \frac{\partial \Psi}{\partial x} + \frac{\partial \tilde{v}_m}{\partial r} \frac{\partial \Psi}{\partial r} + \frac{(m+1)^2}{r^2} \tilde{v}_m \Psi \right) \mathrm{d}xr \, \mathrm{d}r + \hat{B}_T$$
$$- \int_\Omega \hat{p}_m \left(\frac{(1-m)\Psi}{r} + \frac{\partial \Psi}{\partial r} \right) \mathrm{d}xr \, \mathrm{d}r = \int_\Omega \tilde{f}_{m,r} \Psi \, \mathrm{d}xr \, \mathrm{d}r, \tag{50}$$

where Ψ is the test function and $\hat{B}_T$ is the boundary term that results from integration by parts. The SEM discretization proceeds in analogy to the axisymmetric case, i.e., in the elements adjacent to the axis pressure and velocity are discretized at the GLJ and GJ points, respectively. The $1/r$ and $1/r^2$ terms are treated by L'Hôpital's rule as described in Section 3.1, and the boundary conditions of Table 1 are prescribed directly at the axis $r = 0$.

The semi-discretized momentum and continuity equations can be written in matrix form

$$\frac{\partial \underline{\tilde{u}}_m}{\partial t} + \underline{\underline{\tilde{L}}}(m)\underline{\tilde{u}}_m - \underline{\underline{\tilde{D}}}^T(m)\hat{p}_m = \underline{\underline{B}} \, \underline{\tilde{f}}_m, \tag{51}$$

$$\underline{\underline{\tilde{D}}}(m)\underline{\tilde{u}}_m = 0, \tag{52}$$

where

$$\underline{\tilde{u}}_m = (\hat{u}_m, \tilde{v}_m, \tilde{w}_m)^T, \quad \underline{\tilde{f}}_m = (\hat{f}_{m,x}, \tilde{f}_{m,r}, \tilde{f}_{m,\theta})^T.$$

Here $\underline{\underline{\tilde{L}}}(m)$, $\underline{\underline{\tilde{D}}}^T(m)$, and $\underline{\underline{\tilde{D}}}(m)$ represent the discretized diffusion, gradient, and divergence operators corresponding to the mth Fourier mode, respectively. For problems involving variable viscosity, we define $\underline{\underline{\tilde{L}}}^{\max}(m)$ as the discrete diffusion operator related to the maximum viscosity $\mu_{\max}$. We can then employ the semi-implicit BDF2/EX2 scheme described above, see Eqs. (29)–(32). The right-hand-side of the momentum equation involves the discretized form of the non-linear

diffusion operator $\nabla(\mu(x, r, \theta, t)\nabla)\underline{u}$ at the time levels t^n and t^{n-1}. Both this operator as well as the convection operator in the concentration equation are evaluated in a pseudo-spectral fashion [19]. The fractional step method can still be applied for each Fourier mode. Finally, two Helmholtz equations and one pseudo-Laplacian equation have to be solved for each Fourier mode at time step t^{n+1}. This is done by employing the fast diagonalization solver, as described in Section 3.1.

5.2. Results

As a first step, we consider an unstable density stratification involving two fluids of identical viscosities. As observed in the experiments of Kuang et al. [5], the resulting instability develops in a fully three-dimensional fashion. In a subsequent step, we will allow for variable viscosities as well. In order to closely reproduce the experimental conditions, the value of the Péclet number in the simulations, defined by Eq. (9), is set to $Pe = 1.35 \times 10^5$. Similarly to our investigation for miscible flows in a Hele–Shaw cell (cf. [30]), we initially prescribe a steep concentration gradient at $x = 0$ by means of an error function profile. In addition, we superimpose disturbances in the radial and azimuthal directions in order to accelerate the growth of the instability, so that the initial concentration field has the form

$$c(x, r, \theta, 0) = \frac{1}{2}\mathrm{erf}\left\{\frac{x + \varepsilon \sin(\pi r) \cdot \sin(\theta)}{\beta}\right\}.$$

Here β characterizes the thickness of the interfacial region, while ε determines the magnitude of the radial and azimuthal perturbation. For the representative simulation to be discussed in the following, we set the thickness parameter to $\beta = 0.2$ and choose a small disturbance level of $\varepsilon = 10^{-5}$. The azimuthal wavenumber $m = 1$ is selected for the initial concentration perturbation based on a linear stability investigation [31] that shows $m = 1$ to be the dominant mode for the above parameter combination. In Fig. 7 the absolute value of $\max|\hat{u}_m(x, r, t)|$ is shown as a function of t. The figure demonstrates that both modes are amplified exponentially, and that the amplification rate is larger for the azimuthal mode $m = 1$ than for the axisymmetric mode $m = 0$. By assuming disturbances of the form

$$\hat{u}_m(x, r, t) = \hat{u}'_m(x, r)\mathrm{e}^{\sigma(m)t}, \quad m = 0, 1,$$

amplification rates of $\sigma(0) \approx 0.013$ and $\sigma(1) \approx 0.0195$ are obtained. Hence, azimuthal disturbances are seen to dominate over axial ones as long as the amplitudes are small and non-linear interactions can be neglected. It should be noted that the present amplification rates of $\sigma(m) \approx 0.02$ are in the same range as those of three-dimensional perturbations in corresponding Hele–Shaw flows [30]. In order to study the non-linear regime, we carry out a separate simulation with a larger initial perturbation of $\varepsilon = 0.2$. Fig. 8 shows the time evolution of $\max|\hat{u}_m(x, r, t)|$. This large initial disturbance level renders the flow non-linear from the very beginning. The three-dimensional flow structure is depicted in Fig. 9 by means of iso-surfaces of the concentration level $c = 0.5$ at different times. The sinusoidal initial disturbance can still be recognized at $t = 40$. For later times, a finger of lighter fluid is seen to form and rise into the heavier fluid above, with a corresponding finger of the denser fluid falling downwards. Note that far away from the region where these two fingers pass each other, their tips approach the centerline again, so that a nearly axisymmetric flow evolves locally around the tip. For all times, the overall flow is seen to maintain
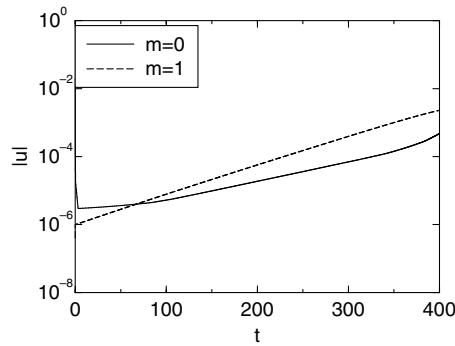
Fig. 7. Absolute value of $\max |\hat{u}_m(x, r, t)|$ for $m = 0, 1$. $Pe = 1.35 \times 10^5$, $\varepsilon = 10^{-5}$. Exponential growth is observed for both the axisymmetric ($m = 0$) and the azimuthal ($m = 1$) mode. However, the azimuthal mode is seen to grow more rapidly, which indicates a three-dimensionally dominated evolution of the flow.
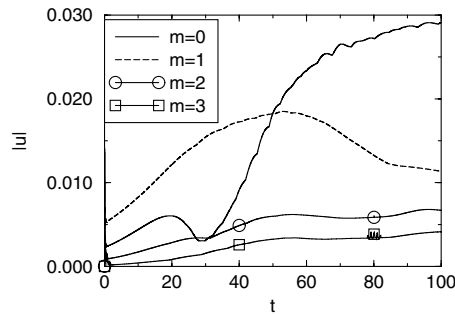

Fig. 8. Absolute value of $\max |\hat{u}_m(x, r, t)|$ for $m = 0, 1, 2, 3$. $Pe = 1.35 \times 10^5$, large initial disturbance level ($\varepsilon = 0.2$).

nearly perfect point symmetry around the origin, as expected on the basis of the symmetry properties of the governing equations. Fig. 10 shows the same flow field from a different perspective.

In a final simulation, we extend the above simulation to fluids of different viscosities. The heavier fluid is assumed less viscous than the lighter fluid below it, with the density contrast given by $At = 0.82$ ($R = 2.3$). The initial conditions are identical to the previous case. Figs. 11 and 12 show the iso-concentration surfaces for three different times. The more viscous, rising finger of lighter fluid is seen to be substantially wider than its less viscous, falling counterpart. Again, both finger tips are seen to assume nearly axisymmetric shapes far above and below the original plane of instability. The symmetry properties of the constant viscosity case are no longer observed. This is in close agreement with the experimental findings of Kuang et al. [5].

6. Summary and conclusions

The purpose of the present investigation is to introduce a highly accurate numerical method for time-dependent, three-dimensional simulations of variable density and viscosity, miscible flows in
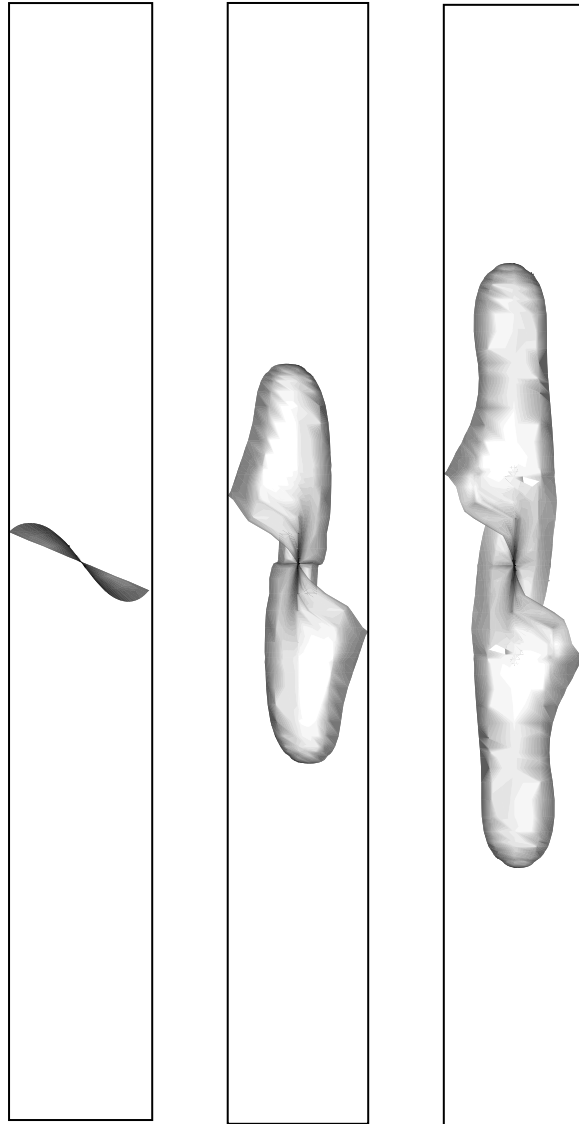
Fig. 9. Temporal evolution of the concentration field for the constant viscosity case. Shown is the $c = 0.5$ isosurface at $t = 40, 200$ and 400. $Pe = 1.35 \times 10^5$.

a cylindrical geometry. Towards this end, we have developed an approach that treats the conservation equations in a cylindrical coordinate system. The spatial discretization is performed by a mixed spectral element/Fourier spectral scheme. Here, the treatment of the well known singularity on the axis of symmetry requires special care. We employ a transformation of the velocity components in Fourier space, which removes the singularity directly at the axis. Moreover, special polynomial expansion functions based on the Jacobi polynomial $P^{(0,1)}$ are used in the first elements adjacent to the axis, in order to obtain a proper behavior of the solution for $r \to 0$. Spectral convergence is demonstrated for the present numerical scheme.
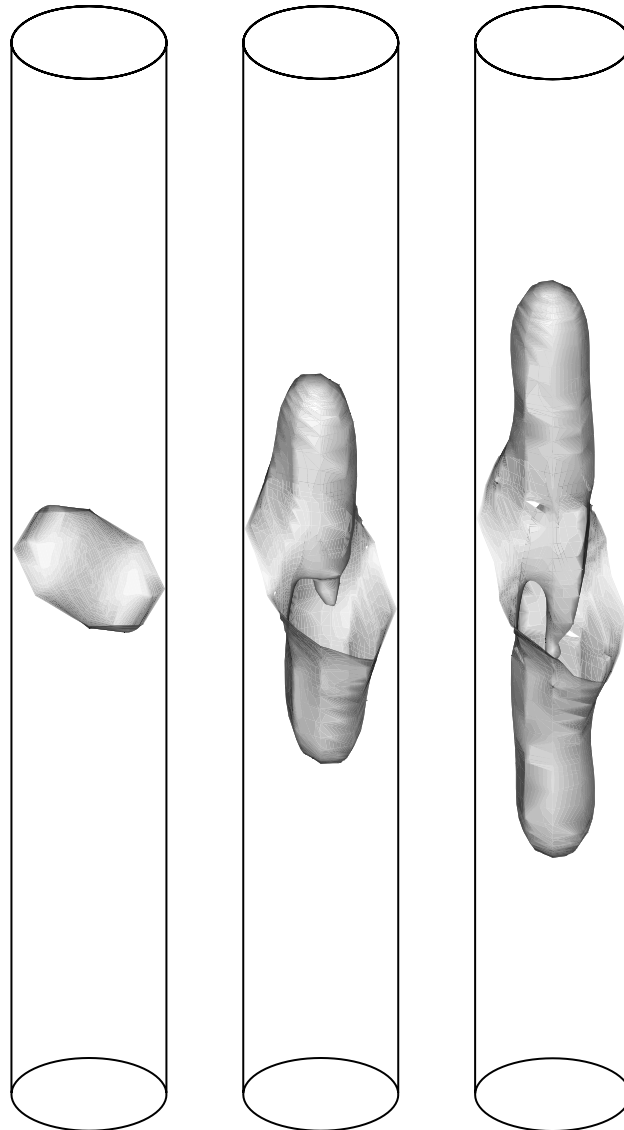
Fig. 10. Temporal evolution of the concentration field for the constant viscosity case. Same results as in Fig. 9, but shown from a different perspective.

The high-accuracy spatial discretization is combined with an efficient semi-implicit time stepping scheme. This approach is especially well-suited for the momentum equation with variable viscosity. It allows for an implicit treatment with a constant diffusion operator, even though the viscosity varies with both location and time. The resulting semi-discretized momentum equation is absolutely stable. While this is not the case for the concentration equation if the convection operator is treated explicitly, the constraint due to the CFL condition is much less severe than that resulting form an explicitly treated diffusion operator. Moreover, all equations are of the
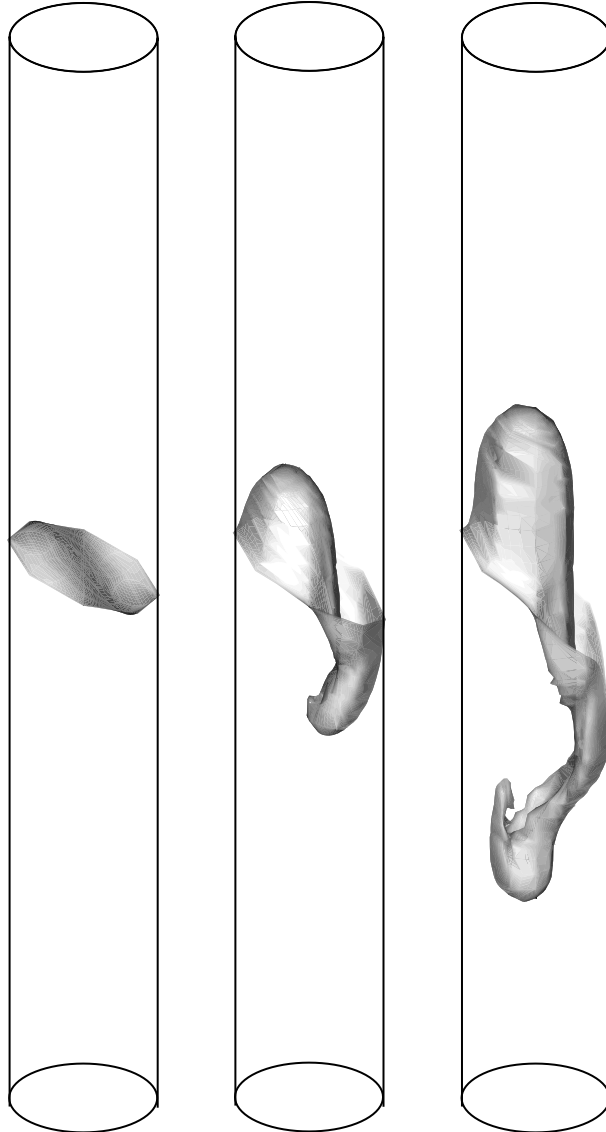
Fig. 11. Temporal evolution of the concentration field for the variable viscosity case. Shown is the $c = 0.5$ isosurface at $t = 10, 50$ and 100. $Pe = 1.35 \times 10^5, R = 2.3$.

Helmholtz type and are solved by a efficient direct solver that is based on a fast diagonalization method.

The above approach has been validated in various ways, and some initial simulations of three-dimensional variable density and viscosity flows have been presented. The results for displacements driven by a net flow are in close agreement with earlier numerical and experimental observations. In addition, the three-dimensionally evolving instability resulting from an unstable
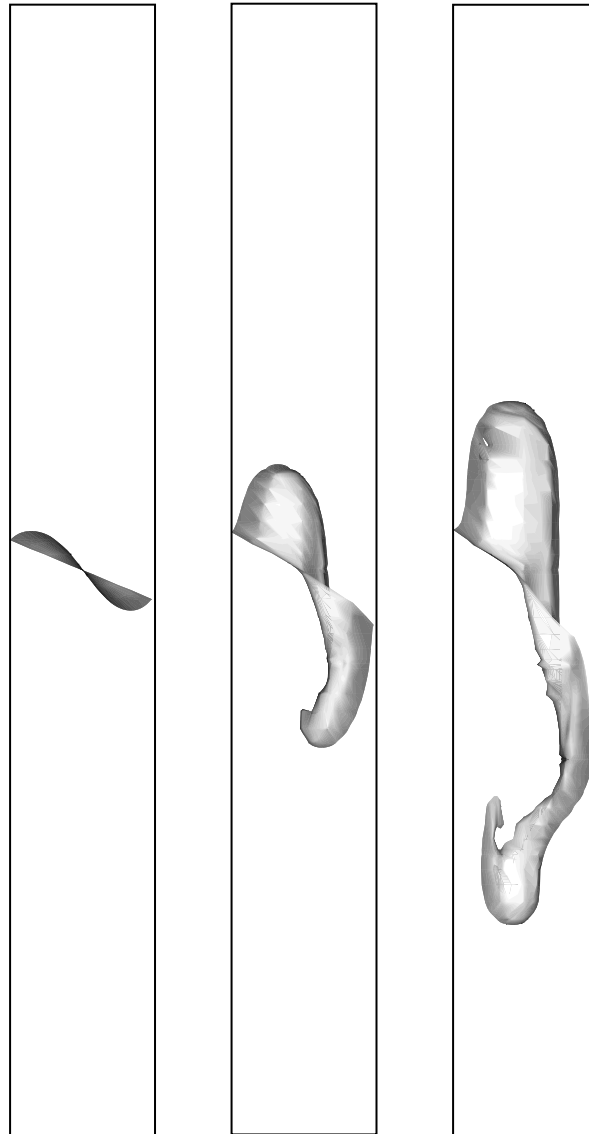
Fig. 12. Temporal evolution of the concentration field for the variable viscosity case. Same results as in Fig. 11, but shown from a different perspective.

density stratification closely resembles experimental observations by Kuang et al. [5]. In particular, for the constant viscosity case a point symmetric structure is observed that is characterized by two symmetric fingers propagating in opposite directions. For the case of variable viscosity, an initially prescribed point symmetry quickly breaks up, and the two emerging fingers assume different shapes. We are now in a position to vary the governing parameters systematically, and to explore the physical coupling between density and viscosity driven mechanisms. The results of this investigation will be reported separately.

Acknowledgements

Appendix A

A.1. Fast diagonalization solver

The fast diagonaliztion solver employed in the present work is based on the method of Lynch et al. [20]. This solver can be used to invert operators L which are constructed from one-dimensional operators L_x and L_r in the following manner:

$$L = [(L_x \otimes I_r) + (I_x \otimes L_r)], \tag{A.1}$$

where $A \otimes B$ denotes the tensor product of the matrices A and B. Lynch et al. [20] showed that the inverse of L is given by

$$L^{-1} = (P_x \otimes P_r)\Lambda^{-1}(P_x^{-1} \otimes P_r^{-1}),$$
$$\Lambda = (\Lambda_x \otimes I_r + I_x \otimes \Lambda_r).$$

The matrices I_x, I_r are the one-dimensional unity matrices corresponding to the derivative operators L_x, L_r. The matrices P_x, P_r contain the eigenvectors of L_x, L_r and Λ_x, Λ_r are the diagonal matrices of the corresponding eigenvalues. With these matrices L_x and L_r can be decomposed as

$$L_x = P_x \Lambda_x P_x^{-1}, \quad L_r = P_r \Lambda_r P_r^{-1}.$$

This decomposition can be performed in a preprocessing step, as long as L is time-independent. On a Cartesian domain, the pressure matrix in Eq. (25) can be written in the from of (A.1) and this method can be applied to solve the pressure equation. The same would be true for a time-independent velocity Helmholtz equation.

A.2. Stability of semi-implicit method

In the following we will show that the semi-implicit method proposed in Section 3.2 is unconditionally stable. For this purpose, we consider the simplified scalar test problem on the interval $\Omega = [-1, 1]$:

$$\frac{\partial u}{\partial t} - \mu(x, t)\frac{\partial^2 u}{\partial x^2} = 0, \tag{A.2}$$

where $\mu(x, t)$ is a positive function on Ω. We define the SEM approximation of the operator $-\mu(x, t)\partial^2/\partial x^2$ by L, and $L^{\max}$ as the SEM approximation of $-\mu_{\max}\partial^2/\partial x^2$, where $\mu_{\max} = \max(\mu(x, t))$ over Ω. The (first order) backward Euler discretization of Eq. (A.2) reads

$$\frac{Bu_N^{n+1} - Bu_N^n}{\Delta t} + Lu_N^{n+1} = 0, \tag{A.3}$$

where u_N^n denotes the discretized velocity at time step $t^n := n \cdot \Delta t$, and B is the diagonal mass matrix of the SEM approximation. Now we add $L^{\max}$ on both sides:

$$\frac{Bu_N^{n+1}}{\Delta t} + L^{\max}u_N^{n+1} = (L^{\max} - L)u_N^{n+1} + \frac{Bu_N^n}{\Delta t},$$

and if we extrapolate the term $(L^{\max} - L)u_N^{n+1}$ first order in time, we obtain

$$(B + \Delta t L^{\max})u_N^{n+1} = [B + \Delta t(L^{\max} - L)]u_N^n.$$

This is equivalent to

$$u_N^{n+1} = \underbrace{[B + \Delta t L^{\max}]^{-1}[B + \Delta t(L^{\max} - L)]}_{:=G} u_N^n.$$

It is obvious that the norm of the matrix G is less or equal 1, because $\|L^{\max} - L\| \leqslant \|L^{\max}\|$, where $\|\cdot\|$ is a given matrix norm. Consequently, the discretization scheme is unconditionally stable. This line of reasoning can easily be extended to higher order schemes such as the second order BDF2/EX2 scheme employed in Section 3.2.

References

[1] Joseph DD, Bai R, Chen KP, Renardy YY. Core-annular flows. Ann Rev Fluid Mech 1997;27:65–90.
[2] Balasubramaniam R, Rashidnia N, Maxworthy T, Alexander JID. Instability of miscible interfaces. Private Communication 2000.
[3] Scoffoni J, Lajeunesse E, Homsy GM. Interface instabilities during displacements of two miscible fluids in a vertical pipe. Phys Fluids 2001;13:553–5.
[4] Petitjeans P, Maxworthy T. Miscible displacements in capillary tubes. Part 1. Experiments. J Fluid Mech 1996;326:37–56.
[5] Kuang J, Maxworthy T, Petitjeans P. Experiments on slow miscible displacement in round tubes. Submitted for publication.
[6] Chen C-Y, Meiburg E. Miscible displacements in capillary tubes. Part 2. Numerical simulations. J Fluid Mech 1996;326:57–90.
[7] Joseph DD, Renardy YY. Fundamentals of two-fluid dynamics. Part 1. Mathematical theory and applications. Berlin: Springer-Verlag; 1993.
[8] Chen C-Y, Meiburg E. Miscible displacements in capillary tubes: Influence of Korteweg stresses and divergence effects. Phys Fluids 2002;14:2052–8.
[9] Ruith M, Meiburg E. Direct numerical simulations of vortex breakdown in three-dimensional swirling flows: Computational boundary conditions. Comp Fluids, in press.
[10] Verzicco R, Orlandi P. A finite-difference scheme for three-dimensional incompressible flows in cylinder coordinates. J Comput Phys 1996;123:402–14.
[11] Le Marec C, Guérin R, Haldenwang P. Collocation method for convective flow induced by directional solidification in a cylinder. Int J Numer Meth Fluids 1996;22:393–409.
[12] Serre E, Pulicani JP. A three-dimensional pseudospectral method for rotating flows in a cylinder. Comput Fluids 2001;30:491–519.
[13] Ma B, van Doorne CWH, Zhang Z, Nieuwstadt FTM. On the spatial evolution of a wall-imposed periodic disturbance in pipe Poiseuille flow at $Re = 3000$. Part 1. Subcritical disturbance. J Fluid Mech 1999;398:181–224.

[14] Tomboulides AG. Direct and large eddy simulation of wake flows: Flow past a sphere. PhD Thesis, Princeton University, 1993.

[15] Tomboulides AG, Orszag SA. Numerical investigation of transitional and weak turbulent flow past a sphere. J Fluid Mech 2000;416:45–73.

[16] Maday Y, Patera AT. Spectral element methods for the incompressible Navier–Stokes equations. In: Noor AK, editor. State-of-the-art-surveys in computational mechanics. New York: ASME; 1989. p. 71–143.

[17] Bernardi C, Dauge M, Maday Y. Spectral element methods for axisymmetric domains. Paris: Elsevier; 1999.

[18] Gerritsma MI, Phillips TN. Spectral element methods for axisymmetric Stokes problems. J Comput Phys 2000;164:81–103.

[19] Canuto C, Hussaini MY, Quarteroni A, Zang TA. Spectral methods in fluid dynamics. Heidelberg: Springer-Verlag; 1988.

[20] Lynch RE, Rice JR, Thomas DH. Direct solution of partial difference equations by tensor product methods. Numer Math 1964;6:185–99.

[21] Couzy W, Deville MO. A fast Schur complement method for the spectral element discretization of the incompressible Navier–Stokes equations. J Comput Phys 1995;116:135–42.

[22] Gresho PM. Incompressible fluid dynamics: Some fundamental formulation issues. Ann Rev Fluid Mech 1991;23:413–53.

[23] Karniadakis GE, Israeli M, Orszag SA. High-order splitting methods for incompressible Navier–Stokes equations. J Comput Phys 1991;97:414–43.

[24] Brezzi F, Fortin M. Mixed and hybrid finite element methods. New York: Springer-Verlag; 1991.

[25] Maday Y, Patera AT, Rønquist EM. An operator-integration-factor splitting method for time-dependent problems: Application to incompressible fluid flow. J Sci Comput 1990;5:263–92.

[26] Couzy W. Spectral element discretization of the unsteady Navier–Stokes equations and its iterative solution on parallel computers. Thèsis No. 1380, École Polytechnique Fédéral de Lausanne, 1995.

[27] Wilhelm D. Numerical investigation of three-dimensional separation in a forward-facing step flow using a spectral element method. In: Reihe 7, 404, Düsseldorf: VDI-Verlag; 2001.

[28] Fischer PF. An overlapping Schwarz method for spectral element solution of the incompressible Navier–Stokes equations. J Comput Phys 1997;133:84–101.

[29] Tomboulides AG. Private Communication 2001.

[30] Graf F, Meiburg E, Härtel C. Density-driven instabilities of miscible fluids in a Hele–Shaw cell: Linear stability analysis of the three-dimensional Stokes equations. J Fluid Mech 2002;451:261–82.

[31] Vanaparthy SH, Meiburg E, Wilhelm D. Density-driven instabilities of miscible fluids in a capillary tube: Linear stability analysis. J Fluid Mech, in press.